Quantum Coherence in an Exchange-Coupled Dimer of Single-Molecule Magnets

S. Hill,[1]* R. S. Edwards,[1] N. Aliaga-Alcalde,[2] G. Christou[2]

A multi–high-frequency electron paramagnetic resonance method is used to probe the magnetic excitations of a dimer of single-molecule magnets. The measured spectra display well-resolved quantum transitions involving coherent superposition states of both molecules. The behavior may be understood in terms of an isotropic superexchange coupling between pairs of single-molecule magnets, in analogy with several recently proposed quantum devices based on artificially fabricated quantum dots or clusters. These findings highlight the potential utility of supramolecular chemistry in the design of future quantum devices based on molecular nanomagnets.

Considerable effort has focused on finding building blocks with which to construct the quantum logic gates (qubits) necessary for a quantum computer (1, 2). Most proposals utilizing electronic spin states take advantage of nanofabrication methods to create artificial molecules, or magnetic quantum dots (3, 4). A Heisenberg-type exchange coupling between dots is achieved by allowing the electronic wave functions to leak from one dot to the next. This coupling is the essential ingredient in a quantum device because, unlike classical binary logic, it enables encoding of data via arbitrary superpositions of pure quantum states, e.g., $|0\rangle$ and $|1\rangle$ (2). These superposition states can store information far more efficiently than a classical binary memory. Furthermore, they permit massively parallel computations, i.e., many simultaneous quantum logic operations may be implemented on a single superposition state. For a quantum device to become a viable technology, it should be possible to perform a reasonably large number of quantum operations ($\sim 10^4$) on a single qubit without the superposition states losing phase coherence. Herein lies one of the main technical challenges, because most quantum systems are highly susceptible to decoherence through coupling to their environment (5).

We demonstrate that single-molecule magnets (SMMs) may be assembled to form coupled quantum systems of dimers (or chains, etc.), with many of the attributes of quantum dot–based schemes. Most importantly, our electron paramagnetic resonance (EPR) investigations of crystals (large, highly ordered three-dimensional arrays) containing exchange-coupled dimers of SMMs show that decoherence rates are considerably less than the characteristic quantum splittings ($\Delta/h \sim$ GHz, where Δ is the energy splitting and h is the Planck constant) induced by the exchange couplings within the dimers, representing a step forward in the drive toward potential applications involving molecular magnets. Several proposals have suggested possible quantum computing schemes utilizing molecular magnets (6–8). The supramolecular (or "bottom-up") approach to materials design is particularly attractive, because it affords control over many key parameters required for a viable qubit: Simple basis states may be realized through the choice of molecule; exchange couplings may then be selectively designed into crystalline arrays of these molecules; finally, one can isolate the qubits to some degree by attaching bulky organic groups to their periphery.

The subject of this investigation is the compound $[Mn_4O_3Cl_4(O_2CEt)_3(py)_3]_2 \cdot 2C_6H_{14}$ (hereafter $[Mn_4]_2$; $EtCO_2^-$ is propionate, py is pyridine, and C_6H_{14} is hexane) (9), a member of a growing family of Mn_4 complexes that act as SMMs (10, 11), having a well-defined ground-state spin of $S = 9/2$. This compound crystallizes in a hexagonal space group ($R\bar{3}$) with the Mn_4 molecules lying head-to-head on a crystallographic S_6 axis. The resulting $[Mn_4]_2$ supramolecular dimer is held together by six weak $C-H \cdots Cl$ hydrogen bonds (Fig. 1), leading to an appreciable antiferromagnetic superexchange coupling ($J \sim 10$ µeV) between the Mn_4 units within the dimer, which influences the low-temperature quantum properties of related $[Mn_4]_2$ dimers (12). Like all SMMs, $[Mn_4]_2$ displays superparamagnetic-like behavior at high temperatures, and magnetic

hysteresis below a characteristic blocking temperature (~ 1 K). The hysteresis loops exhibit steps, which are due to magnetic quantum tunneling (MQT). However, unlike isolated SMMs, there is an absence of MQT at zero-field, due to a static exchange bias field that each molecule experiences because of its neighbor within the dimer (12). The effect of the bias is to shift the field positions of the main MQT steps by an amount of order $-JS^2/\mu$ (where µ is the magnetic moment of a Mn_4 monomer), so that the first step is observed on the hysteresis loop before reaching zero-field. However, the exchange bias by itself does not quantum mechanically couple the SMMs within the dimer.

Before presenting experimental evidence for the coupled nature of the dimers, we develop a quantum mechanical model that takes this coupling into account. Neglecting off-diagonal crystal field terms and intermolecular interactions, the effective spin Hamiltonian (to fourth order) for a magnetic field (B_z) applied parallel to the easy (z) axis of a single isolated SMM has the form (11)

$$\hat{H}_i = D\hat{S}_{zi}^2 + B_4^0 \hat{O}_4^0 + g_z \mu_B B_z \hat{S}_{zi} \quad (1)$$
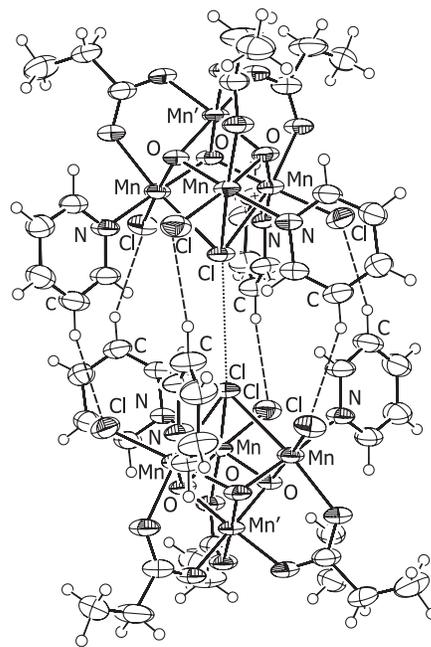
where $\hat{S}_{zi}$ is the z-axis spin projection opera-

Fig. 1. The $[Mn_4O_3Cl_4(O_2CEt)_3(py)_3]_2$ dimer; the Mn^{3+} and Mn^{4+} ions are labeled Mn and Mn', respectively. The dashed lines represent the $C-H \cdots Cl$ hydrogen bonds holding the dimer together, and the dotted line is the close approach of the central bridging Cl atoms believed to be the main pathway for the exchange interaction between the two Mn_4 molecules.

---

[1]Department of Physics, University of Florida, Gainesville, FL 32611, USA. [2]Department of Chemistry, University of Florida, Gainesville, FL 32611, USA.

*To whom correspondence should be addressed. E-mail: hill@phys.ufl.edu

tor, and the index i ($= 1, 2$) is used to label the two Mn_4 molecules in the dimer for the interacting case below; D (<0) is the uniaxial anisotropy constant; $B_4^0 \hat{O}_4^0$ characterizes the fourth-order axial anisotropy; and g_z is the z-component of the Landé g-tensor. The omission of transverse terms in Eq. 1 does not affect the EPR spectra (they merely result in weak avoided level crossings, which cause the MQT).

For the case of two quantum mechanically coupled SMMs, the effective dimer Hamiltonian ($\hat{H}_D$) may be separated into the following diagonal and off-diagonal terms
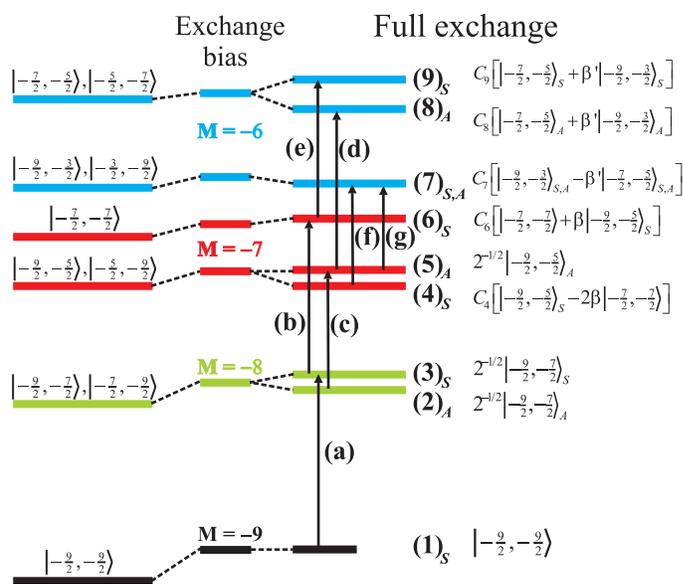
$$\hat{H}_D = [\hat{H}_1 + \hat{H}_2 + J_z \hat{S}_{z1} \hat{S}_{z2}] +$$
$$\left\{ \frac{1}{2} J_{xy} \left(\hat{S}_1^+ \hat{S}_2^- + \hat{S}_1^- \hat{S}_2^+ \right) \right\} \quad (2)$$

where $\hat{H}_1$ and $\hat{H}_2$ are given by Eq. 1, the cross terms describe the exchange coupling between the two SMMs within the dimer, and the J values characterize the strength of this coupling. The diagonal zeroth-order Hamiltonian ($\hat{H}_{0D}$, in square brackets) includes the exchange bias $J_z \hat{S}_{z1} \hat{S}_{z2}$, which has been considered previously (12). The zeroth-order eigenvectors for the dimer may be written as products of the single-molecule eigenvectors $|m_1\rangle$ and $|m_2\rangle$ (abbreviated $|m_1, m_2\rangle$), where m_1 and m_2 represent the spin projections of the two molecules within the dimer. The zeroth-order eigenvalues are then easily obtained by solving Eq. 1 separately for molecules 1 and 2, and adding the exchange bias $J_z m_1 m_2$ (Fig. 2).

In EPR, the only effect of the exchange bias is to cause shifts in the positions (energies) of single-spin transitions ($m_i \rightarrow m_i \pm 1$), with the magnitude of the shift (bias) depending on the state m_j of the other molecule within the dimer. The off-diagonal interaction in Eq. 2 ($\hat{H}_D'$ in curly brackets) couples the molecules, giving rise to the possibility of single-photon transitions between coupled states of the dimer. In principle, one could observe this coupling in hysteresis measurements, because magnetic relaxation mediated by tunneling into distinct superposition states occurs at slightly different magnetic field strengths, even when the tunneling occurs via states with the same total spin projection ($= m_1 + m_2$). However, the predicted splittings of MQT resonances turn out to be less than the inhomogeneous linewidths of the hysteresis steps (12). Thus, clear evidence for the coupled nature of the dimer system has so far been lacking.

For illustrative purposes, we treat $\hat{H}_D'$ perturbatively. Because this interaction conserves angular momentum, the eigenvectors may be grouped into multiplets based on the sum of the projections $M = m_1 + m_2$. $\hat{H}_D'$

Fig. 2. Schematic showing the lowest energy states ($M = -9$ to -6, not to scale) of the dimer: The zeroth-order energy levels and eigenvectors are shown on the left; energy shifts due to the exchange bias are shown in the center; and the results of a full quantum calculation (Eq. 2) are displayed on the right. The colors denote the total angular momentum (M) state of the dimer, and the levels have been numbered to aid discussion. Several of the strongest EPR transitions are indicated by arrows [(a) through (g)]. The corrected eigenvectors are listed next to each state: based on the deduced value of J (see main text), $\beta = 0.400$ and $\beta' = 0.231$; the subscripts S and A (on a state $|m_1, m_2\rangle$) denote symmetric and antisymmetric combinations of $|m_1, m_2\rangle$ and $|m_2, m_1\rangle$, respectively; the C coefficients are normalization constants.

then acts only between states within a given multiplet. The zeroth-order eigenvectors are grouped according to this scheme in Fig. 2 (left). In first order, $\hat{H}_D'$ acts between zeroth-order eigenvectors $|m_1, m_2\rangle$ and $|m_1 \pm 1, m_2 \mp 1\rangle$. The effect of this first-order interaction is most apparent in the $M = -8$ multiplet, where it lifts the degeneracy between the $|-(9/2), -(7/2)\rangle$ and $|-(7/2), -(9/2)\rangle$ states. The resultant eigenvectors correspond to symmetric (S) and antisymmetric (A) superpositions of the original product states. Indeed, $\hat{H}_D'$ causes considerable mixing of the zeroth-order eigenvectors within all multiplets, resulting in the first-order corrected eigenvectors, which are listed in Fig. 2 (right) for the lowest four multiplets; here, $|m_1, m_2\rangle_S$ implies ($|m_1, m_2\rangle + |m_2, m_1\rangle$) and $|m_1, m_2\rangle_A$ implies ($|m_1, m_2\rangle - |m_2, m_1\rangle$).
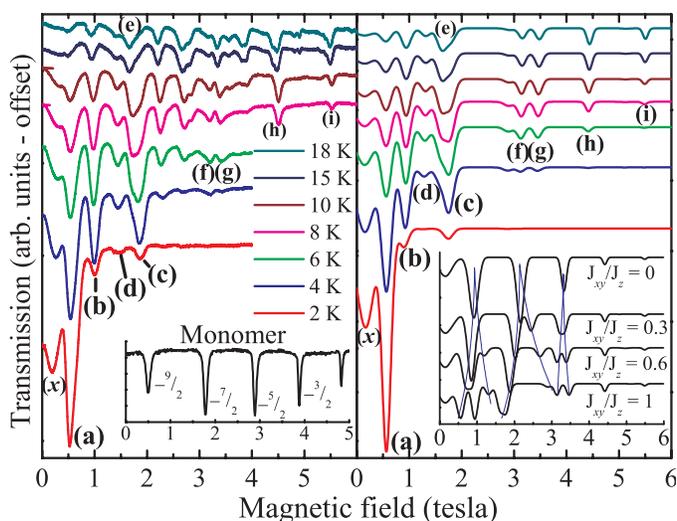
In Fig. 2, we display a schematic of the energy-level shifts and splittings (not to scale) caused by the exchange bias, and by the full exchange, for the lowest lying levels at high magnetic fields ($M = -9$ to -6). The states are numbered for convenient discussion of the data. For clarity, higher lying states with $M > -6$, including the zero-field $|\pm(9/2), \mp(9/2)\rangle$ ground states, are not shown in Fig. 2. Application of a magnetic field parallel to the easy axis merely shifts all of the zeroth-order levels by an amount $g \mu_B B_z M$. Thus, $\delta M = \pm 1$ EPR transition matrix elements may be accurately calculated using the eigenvectors in Fig. 2. The magnetic dipole perturbation only allows transitions between states having the same symmetry. The strongest of these transitions are shown in Fig. 2, labeled (a) through (g).

In the left panel of Fig. 3, we display

temperature-dependent high-frequency EPR spectra obtained at 145 GHz, with the magnetic field applied parallel to the easy axis of a small (<1 mm³) single-crystal sample; details of our high-frequency EPR setup are given elsewhere (13). The inset shows a single 6 K spectrum ($f = 140$ GHz) for a related monomeric Mn_4 complex without head-to-head interactions (14). The monomer data are typical of most SMMs, showing a series of more-or-less evenly spaced resonances, and a smooth variation in intensity from one peak to the next. By contrast, the dimer spectra exhibit considerable complexity. Despite this complexity, the simulated dimer spectra (colored traces in the right panel of Fig. 3) show marked agreement with the raw data, both in the peak positions and relative intensities. The optimum parameters were deduced from a single fit to Eq. 2 of the main EPR peak positions obtained at many microwave frequencies. This fit, displayed in Fig. 4, yields the following values: $D = -0.750(15)$ K, $B_4^0 = -5(2) \times 10^{-5}$ K, $g_z = 2$, and $J = 0.12(1)$ K. These crystal field parameters are very similar to those obtained for the monomer [$D = -0.7$ K, $B_4^0 = -9 \times 10^{-5}$ K (14)]. We did not find it necessary to include anisotropy in the superexchange coupling for the dimer (i.e., $J_z = J_{xy} = J$), although long-range dipolar interactions improved the quality of the fit (15, 16).

The simulated spectra (Fig. 3) are mainly limited to transitions among the levels displayed in Fig. 2 [(a) through (g)]; we have also included the $(7)_{S,A} \rightarrow |-(9/2), -(1/2)\rangle$ and $|-(9/2), -(1/2)\rangle \rightarrow |-(9/2), +(1/2)\rangle$ transitions, labeled (h) and (i), respectively. Resonance (x), meanwhile, corresponds to

Fig. 3. (**Left**) Temperature-dependent easy-axis data obtained for the $[Mn_4]_2$ dimer at 145 GHz (the dips in transmission correspond to EPR). The inset (black trace) shows a single 6 K, 140 GHz spectrum obtained for a monomeric Mn_4 complex [the resonances are labeled according to the m states from which the transitions were excited (*14*)]. (**Right**) Simulations of the dimer data. The inset illustrates the effect of the transverse part of the exchange (J_{xy}) for four values of J_{xy}/J_z ($T = 8$ K). In both panels, resonances (a) through (g) correspond to the labeled transitions in Fig. 2; resonances (x), (h), and (i) are discussed in the main text. A Gaussian distribution in D ($\sigma_D \sim 1\%$) was included in the simulations to obtain realistic lineshapes (*15*).
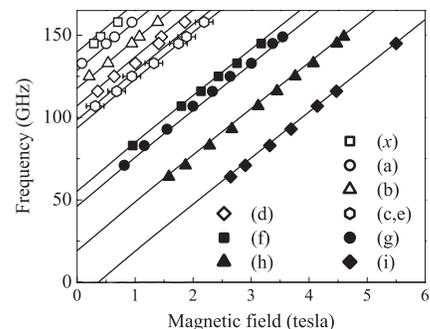
Fig. 4. A single fit to Eq. 2 of the positions of EPR peaks obtained at several frequencies. The optimum Hamiltonian parameters were obtained from this fit. The transitions have been labeled for comparisons with Figs. 2 and 3.

the degenerate $|+(9/2), -(9/2)\rangle \rightarrow |+(9/2), -(7/2)\rangle$ and $|-(9/2), +(9/2)\rangle \rightarrow |-(7/2), +(9/2)\rangle$ transitions. The only significant differences between the experimental data and simulated spectra are seen in the 2 to 3 T region, because we did not consider several moderately strong transitions involving higher lying ($M > -6$) states. We deliberately avoid reference to superposition states in discussing resonance (x), because the interaction between the $|\pm(9/2), \mp(9/2)\rangle$ states is extremely weak (9th order in $\hat{H}'_D$). Consequently, even the weakest coupling to the environment would likely destroy any coherence associated with the $2^{-1/2}|+(9/2), -(9/2)\rangle_{S,A}$ superposition states.

Resonance (x) is observed only over a narrow low-field region (<0.7 T) over which the $|\pm(9/2), \mp(9/2)\rangle$ levels represent the ground states of the dimer. By following the relative intensities of resonances (x) and (a), one obtains an independent thermodynamic estimate of the exchange bias that is in excellent agreement with the value obtained above, and with independent hysteresis measurements for the same complex (*17*). We note that the previously published measurements of the exchange bias in $[Mn_4]_2$ involved a slightly different solvent of crystallization, the full compound having the form $[Mn_4O_3Cl_4(O_2CEt)_3(py)_3]_2 \cdot 8MeCN$ (*9*, *12*). EPR studies for this complex (*14*) show fewer transitions from excited levels [transitions (x), (a), (b), and (c) remain clearly visible]. Nevertheless, one can still estimate a coupling constant [$J = 0.10(1)$ K] from the exchange bias, which is in agreement with the published value (*12*).

The inset to the right panel of Fig. 3 shows that it is the transverse part of the exchange ($\hat{H}'_D$) that brings the simulations into excellent agreement with the data. Indeed, there is no way to obtain anything closely resembling the experimental data without including $\hat{H}'_D$ in the calculation, thus providing compelling evidence that the molecules are coupled quantum mechanically. The issue of quantum coherence is best illustrated by examining the splitting of resonances (f) and (g)—this splitting is directly proportional to J_{xy} and corresponds to the ~9 GHz shift of the $(4)_S$ level relative to $(5)_A$ (Fig. 2). If the phase decoherence rate ($\tau_\phi^{-1} \equiv$ characteristic rate associated with the collapse of a quantum mechanical superposition state) were to exceed 9 GHz, one would expect broad EPR peaks because of transitions between bands of incoherent states; these bands would occupy the gaps between the energies given by the exchange bias picture and the full exchange calculation in Fig. 2, thereby smearing out most of the sharp features in the observed spectrum. In principle, τ_ϕ is the same as the transverse spin relaxation time T_2, which can be estimated from EPR linewidths ($\Delta M = \pm 1$ transitions) (*18*). However, we know that these widths are dominated by weak dimer-to-dimer variations (strains) in the Hamiltonian parameters, i.e., the actual τ_ϕ^{-1} is buried within the inhomogeneous EPR linewidths (*14–16*) and is probably much less than 9 GHz. As a worst case, the narrowest EPR lines would imply a decoherence time on the order of 1 ns. To determine the real T_2 ($\equiv \tau_\phi$), one should carry out time-resolved (pulsed) EPR experiments, e.g., the free-

induction-decay of an initially saturated EPR transition, or Rabi spectroscopy (*18*). Time-resolved experiments in this frequency range are technically challenging but, nevertheless, represent a future objective.

The magnitudes of the quantum splittings (in frequency units) provide a rough estimate of the rates at which one could perform computations. In comparison to many competing technologies [e.g., NMR (*19*)] these rates are high for electronic spin states, i.e., GHz rather than kHz or MHz. The largest quantum splittings (Δ/h) for the dimer are on the order of a few tens of GHz. In fact, $\Delta\tau_\phi/h$ represents a rough figure of merit for a quantum device, because it gives an estimate of the number of qubit operations one could perform without loss of phase coherence. For the worst case given above, $\Delta\tau_\phi/h \sim 30$ to 100; in reality, it may well be 10^4 or greater. The most useful coupled states of the dimer would be the antiferromagnet zero-field $2^{-1/2}|+(9/2), -(9/2)\rangle_{S,A}$ ground states, or Bell states (*2*). As already discussed, the tunnel splitting of these states is negligible in zero-field ($\sim$ Hz). However, it is possible to increase this splitting to a practical range ($\sim$GHz) with a transverse magnetic field. Although there remain technical challenges along the road map toward molecule-based quantum devices (e.g., low operating temperatures, methods for addressing nanometer-sized molecules, etc.), the present study demonstrates that the "bottom-up" (molecular) approach provides excellent opportunities to study coherent quantum superposition states. Future materials design strategies will, therefore, explore the following possibilities: optical control of the exchange coupling between the two halves of a dimer; increased isolation of the dimers to further reduce decoherence; and the inclusion of some form of asymmetry within the dimer (e.g., uncompensated electronic spins, or selective nuclear spin labeling), thereby facilitating readout of the state of the system.

References and Notes

1. D. P. DiVincenzo, D. Loss, *J. Magn. Magn. Mater.* **200**, 202 (1999).
2. M. A. Nielsen, I. L. Chuang, *Quantum Computation and Quantum Information* (Cambridge, New York, 2000).
3. D. P. DiVincenzo, D. Bacon, J. Kempe, G. Burkard, K. B. Whaley, *Nature* **408**, 339 (2000).
4. G. Burkard, H.-A. Engel, D. Loss, *Fortschr. Phys.* **48**, 965 (2000).
5. M. Dube, P. C. E. Stamp, *Chem. Phys.* **268**, 257 (2001).
6. S. C. Benjamin, S. Bose, *Phys. Rev. Lett.* **90**, 247901 (2003).
7. M. N. Leuenberger, D. Loss, *Nature* **410**, 789 (2000).
8. F. Meier, J. Levy, D. Loss, *Phys. Rev. B* **68**, 134417 (2003).
9. D. N. Hendrickson *et al.*, *J. Am. Chem. Soc.* **114**, 2455 (1992). The present compound was prepared by the same procedure, but crystallized from dichloromethane/diethyl ether/hexanes, instead of acetonitrile.
10. G. Christou, D. Gatteschi, D. N. Hendrickson, R. Sessoli, *MRS Bull.* **25**, 66 (2000).
11. D. Gatteschi, R. Sessoli, *Angew. Chem.* **42**, 268 (2003).
12. W. Wernsdorfer, N. Aliaga-Alcalde, D. N. Hendrickson, G. Christou, *Nature* **416**, 406 (2002).
13. M. M. Mola, S. Hill, P. Goy, M. Gross, *Rev. Sci. Instrumen.* **71**, 186 (2000).
14. R. S. Edwards *et al.*, *Polyhedron* **22**, 1911 (2003).
15. K. Park, M. A. Novotny, N. S. Dalal, S. Hill, P. A. Rikvold, *Phys. Rev. B* **65**, 14426 (2002).
16. S. Hill *et al.*, *Phys. Rev. B* **66**, 224410 (2002).
17. W. Wernsdorfer, personal communication.
18. A. Schweiger, G. Jeschke, *Principles of Pulsed Electron Paramagnetic Resonance* (Oxford Univ. Press, Oxford, 2001).
19. W. S. Warren, N. Gershenfeld, I. Chuang, *Science* **277**, 1688 (1997).
20. We thank W. Wernsdorfer for useful discussion. This work was supported by the NSF and by Research Corporation.

Mars-Like Soils in the Atacama Desert, Chile, and the Dry Limit of Microbial Life

Rafael Navarro-González,[1,2]* Fred A. Rainey,[3] Paola Molina,[1]
Danielle R. Bagaley,[3] Becky J. Hollen,[3] José de la Rosa,[1]
Alanna M. Small,[3] Richard C. Quinn,[4,5] Frank J. Grunthaner,[6]
Luis Cáceres,[7] Benito Gomez-Silva,[8] Christopher P. McKay[5]

The Viking missions showed the martian soil to be lifeless and depleted in organic material and indicated the presence of one or more reactive oxidants. Here we report the presence of Mars-like soils in the extreme arid region of the Atacama Desert. Samples from this region had organic species only at trace levels and extremely low levels of culturable bacteria. Two samples from the extreme arid region were tested for DNA and none was recovered. Incubation experiments, patterned after the Viking labeled-release experiment but with separate biological and nonbiological isomers, show active decomposition of organic species in these soils by nonbiological processes.

The results of the Viking lander analyses of soils on Mars are puzzling in three respects. First is the absence of organic materials at the level of parts-per-billion (ppb), as measured by pyrolysis–gas chromatography–mass spectrometry (pyr-GC-MS) (*1*, *2*). The second unexpected result is the rapid release of molecular oxygen, at levels of 70 to 770 nmol g^{-1}, when soil samples were exposed to water vapor in the gas exchange experiment (*3*).

The third puzzling result is that organic material in the labeled-release (LR) experiment was consumed as expected if life were present (*4*) (supporting online text). However, the presence of life is in apparent contradiction with the results from pyr-GC-MS. Currently, the most widely accepted explanation for the reactivity of the martian soil is the presence of one or more inorganic oxidants (such as superoxides, peroxides, or peroxynitrates) at the parts-per-million (ppm) level, whereas the lack of organics can be explained by their oxidation because of the presence of such oxidants and/or by direct ultraviolet radiation damage (*5*) (supporting online text).

We report here results of studies on the soils in the Atacama Desert, an environment that serves as a model for Mars. The Atacama is an extreme, arid, temperate desert that extends from 20°S to 30°S along the Pacific coast of South America (*6–9*) (supporting online text). Soil samples were collected along the precipitation gradient in a north-to-south transect centered on ~70°W between 24°S and 28°S (Fig. 1). They were analyzed (*10*) for organic matter by pyr-GC-MS at 750°C under an inert atmosphere and for the presence of viable heterotrophic microorganisms by serial dilution plating on a number of

artificial culture media that contained high and low nutrient levels. The diversity of the bacterial communities in a number of the samples was investigated by isolation of the total DNA, then polymerase chain reaction (PCR) amplification and sequence determination of the 16S ribosomal RNA (rRNA) genes recovered.

Analysis of samples by pyr-GC-MS revealed that the most arid zone of the Atacama, the Yungay area, is depleted of most organic molecules. Only two peaks in the chromatograms corresponding to organic molecules (formic acid and benzene) are detectable (figs. S1 and S2). In contrast, a less arid site, AT01-22, releases a complex mixture of organic compounds on pyrolysis (fig. S2). We carried out a comparative analysis by pyr-GC-MS with major classes of biomolecules (proteins, carbohydrates, fatty acids, porphyrins, and DNA) and bacterial mass (e.g., strain AT01-3 isolated from the Atacama Desert) (supporting online text). We concluded that site AT01-22 contains bacteria and/or all of the major classes of biomolecules at levels within the detection limits of the pyr-GC-MS protocol applied.

The two characteristic compounds released by all pyrolysates are formic acid, a highly oxidized organic compound, and benzene, a thermally stable aromatic compound. These two compounds are typically released by the thermal treatment of monocarboxylic acids, polycarboxylic acids, carbohydrates, polysaccharides, amino acids, and proteins. Formic acid is present at concentrations of ~1 μmol g^{-1} in the Yungay area, then decreases by an order of magnitude at 26°S and increases again in the less arid zone (Fig. 2C). In contrast, benzene is present at trace levels (~0.01 μmol g^{-1}) at ~24°S, with its concentration increasing to ~1 μmol g^{-1} in the less arid zone (~28°S). The ratio between formic acid and benzene reaches its highest value (≥12 units) in the Yungay area, and then sharply drops to ≤0.3 from 25°S to 28°S (Fig. 2D). A high formic acid/benzene ratio indicates that the organic matter present in the region is oxidized and possibly composed of refractory organics such as aliphatic and aromatic mono- and polycarboxylic acids.

[1]Laboratorio de Química de Plasmas y Estudios Planetarios, Instituto de Ciencias Nucleares, Universidad Nacional Autónoma de México, Circuito Exterior, Ciudad Universitaria, Apartado Postal 70-543, Mexico City, 04510, Mexico. [2]Laboratoire Inter-Universitaire des Systèmes Atmosphériques, Unité Mixte de Recherche CNRS 7583, Universités Paris 12 et Paris 7, 61 Avenue du Général de Gaulle, F 94010 Créteil Cedex, France. [3]Department of Biological Sciences, 202 Life Sciences Building, Louisiana State University, Baton Rouge, LA 70803, USA. [4]SETI Institute, [5]Space Science Division, NASA Ames Research Center, Moffett Field, CA 94035–1000, USA. [6]NASA Jet Propulsion Laboratory, Pasadena, CA 91109, USA. [7]Instituto del Desierto y Departamento de Ingeniería Química, Facultad de Ingeniería, [8]Instituto del Desierto y Unidad de Bioquímica, Departamento Biomédico, Facultad Ciencias de la Salud, Universidad de Antofagasta, Post Office Box 170, Antofagasta, Chile.

*To whom correspondence should be addressed. E-mail: navarro@nuclecu.unam.mx